Surrogate-based optimization of microstructural features of structural materials

Toda, Hiroyuki
Department of Mechanical Engineering, Kyushu University

Li, Han
Department of Mechanical Engineering, Kyushu University

Batres, Rafael
Campus Cuernavaca, School of Engineering and Sciences, Tecnológico de Monterrey

Fujihara, Hiro
Department of Mechanical Engineering, Kyushu University

出版情報：Acta Materialia. 257 (15), pp.119188-, 2023-09-15. Elsevier
バージョン：

Acta Materialia 257 (2023) 119188

Contents lists available at ScienceDirect

Acta Materialia

journal homepage: www.elsevier.com/locate/actamat

Surrogate-based optimization of microstructural features of structural materials

Hiroyuki Toda [a,*], Han Li [a,b], Rafael Batres [c], Kyosuke Hirayama [a,d], Hiro Fujihara [a]

[a] Department of Mechanical Engineering, Kyushu University, 744, Motooka, Nishi Ward, Fukuoka City, Fukuoka 819-0395, Japan
[b] College of Informatics, Huazhong Agricultural University, 1, Shizishan Jie, Hongshan Qu, Wuhan 430070, China
[c] Campus Cuernavaca, School of Engineering and Sciences, Tecnológico de Monterrey, Av. Eugenio Garza Sada 2501 Sur, Tecnológico, Monterrey, N L 64849, Mexico
[d] Department of Materials Science and Engineering, Kyoto University, Yoshida Honmachi, Sakyo-ku, Kyoto 606-8501, Japan

ARTICLE INFO

Keywords:
Micro-tomography
Particle damage
Surrogate model
Data coarsening
Finite element simulation
Image-based numerical simulation

ABSTRACT

This paper proposes a methodology for surrogate-based microstructural optimization of structural metals that integrates a limited number of 3D image-based numerical simulations with microstructural quantification, coarsening and optimisation processes. The support vector machine that was used had an infill sampling criterion to reduce the number of numerical trials, and the proposed methodology was found to be effective for wrought 2024 aluminium alloy with irregularly shaped particles. Appropriate objective functions were defined to assess particle damage. The number of design parameters, which quantitatively express the size, shape, and spatial distribution of particles, was initially 41, but they were reduced to four during a two-step coarsening process. The surrogate model provided highly accurate predictions, and the size, shape, and spatial distribution values of the optimal and weakest particles were successfully identified. It was shown that the optimal particle was small, spherical, sparsely dispersed, and perpendicular to the loading direction. However, it was also found that the smallest and most independent particle with a spherical shape was not necessarily strong, which implies the effects of particle clustering. It was also concluded that the dependency of in-situ particle strength on size was of crucial importance for weaker particles. The shape and spatial distribution of stronger particles were, however, more crucial for suppressing their internal stress than was their size. The results show that the proposed methodology offers a cost-efficient solution for microstructural designs involving 3D high-fidelity simulations that cannot be obtained with the existing approaches for developing materials.

1. Introduction

Recent laboratory-based and synchrotron X-ray micro- and nano-tomography techniques can readily depict the morphology of microstructural features, such as particles, defects, damage, and crystallographic grains in practical structural metals in full 3D complexity. The spatial resolution of X-ray tomography (XCT) readily reaches the level of the microstructural features of structural materials (e.g., 1 μm) in both laboratory-based and synchrotron XCT techniques [1,2]. X-ray lens-based systems aim to produce more magnified images on a detector, and the spatial resolution has been further improved by an order of magnitude [1,3]. Typically, in the case of the synchrotron X-ray, it is achieved using a lens specially designed for X-rays, which is called the Fresnel zone plate [1,3]. Nowadays, even industrial XCT scanners can be equipped with Fresnel zone plates for high magnification observations. For example, a Fresnel zone plate with an outermost zone width of 35 nm was used to achieve a nominal maximum spatial resolution of 50 nm [1,3]. Although the grain boundaries of structural metal materials cannot be directly visualized even with such X-ray-magnifying optics, techniques that apply X-ray diffraction (e.g. the 3D-XRD [1,4] and DCT techniques [1,5]) or those that combine XCT and X-ray diffraction (e.g. the DAGT technique [1,6]) are available for visualising crystallographic grains in 3D.

The use of 3D image-based numerical simulations is becoming increasingly important compared to conventional analytical and empirical modelling or simulations with simplified and symmetrized models. This is due to the trend toward accurate predictions of mechanical behaviour under external stimuli that can be used to design new products or materials with superior properties. In this aspect, 3D imaging modalities involving XCT enable the creation of high-quality

* Corresponding author.
E-mail address: toda@mech.kyushu-u.ac.jp (H. Toda).

https://doi.org/10.1016/j.actamat.2023.119188
Received 20 January 2023; Received in revised form 12 July 2023; Accepted 24 July 2023
Available online 28 July 2023

numerical models by directly converting 3D high-fidelity tomographic volumes into fine 3D meshes for numerical simulations. The fields of application include automotive design [7], fluid dynamics [8], materials engineering [9–11], etc. Since structural metal materials have distinct boundaries at the nanoscopic level between the internal microstructures and the matrix, this technique can accurately represent the internal microstructures after readily segmenting dissimilar phases.

However, high-fidelity 3D image-based numerical simulations are very time consuming in terms of model preparation and are computationally expensive [1], sometimes requiring a few days or even weeks per single execution after laborious mesh clean-ups, stitching, and debugging that can take a few months. When a limited number of 3D image-based numerical simulations are utilised for the interpretation of some physical phenomenon, such as identifying the origin of damage evolution or obtaining clues for inferior mechanical properties, it is not such a serious issue. The irregular and complex 3D microstructural features of real-world practical materials mean that no two microstructural patterns of an identical material are alike. This is because the formation of microstructural patterns is more or less probabilistic in nature. Therefore, when optimal microstructures are required, 3D image-based numerical simulations should be repeated many times for a single material. But while it is necessary to prepare and compute a number of high-fidelity 3D models, it is, in fact, unrealistic since uncertainties inevitably arise in the final optimisation results due to temporal constraints. This results in inaccuracies and limited reproducibility of the analysis, and the predicted optimisation is unrepresentative of the mechanical behaviour that occurs in actual materials.

One effective way to address the issue of uncertainty is to employ a surrogate model to approximate the relationship between the irregular microstructural patterns for input and the mechanical properties for output. This paper proposes a methodology for surrogate-based optimization of the mechanical properties of structural metals that integrates a limited number of high-fidelity 3D image-based numerical simulations and their high-fidelity quantification. It also reduces the number of microstructural parameters (design parameters) that arise from subsequent coarsening processes, and the final optimisation and assessment is performed with a surrogate model. In this paper, the support vector machine used had an infill sampling criterion that effectively alleviated the computational burden by reducing the number of numerical trials needed to find the final solution.

2. Optimisation methods

This section provides an overview of the methodology for accelerating surrogate-based optimization of 3D image-based numerical simulations. We describe a new method called reverse 4D materials engineering (R4ME), which was inspired by reverse engineering (RE). RE technology is generally defined as the process of analysing an

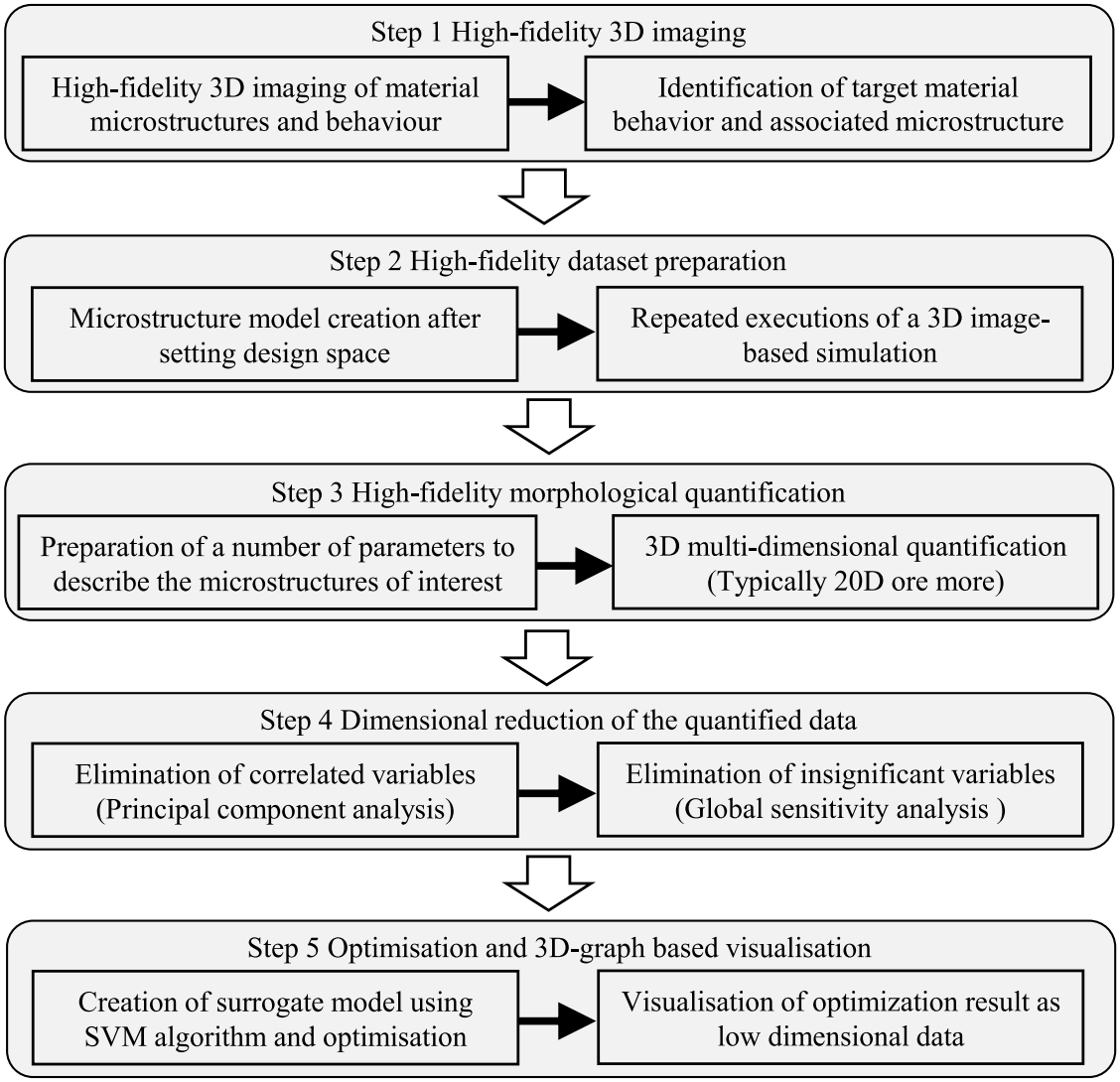

Fig. 1. Methodology for the surrogate-based optimization, which is called reverse 4D materials engineering.

industrial product using software to identify its components and mechanisms so as to redesign it [12]. RE technology enables creating engineering designs along a flow, starting from an existing product toward its design, with a high degree of efficiency. Usually it is orientated from design to products, which is why it is designated as "reverse".

Similarly, in the R4ME process shown in Fig. 1, we approached the relationship between the irregular and complex 3D microstructural features of a real-world practical material and its mechanical responses, such as strength, ductility, toughness, fatigue properties, and susceptibility to damage, starting from visualising the irregular and complex microstructural features of an existing practical material in 3D (Step 1 in Fig. 1) toward its optimal design (Step 5 in Fig. 1). Because the complexity of the 3D image makes this analysis theoretically intractable, we performed an image-based numerical simulation with a high-fidelity 3D model (Step 2 in Fig. 1). The simulation provided us with the relationship between the microstructures and the macroscopic (or sometimes mesoscopic or microscopic) responses of the materials being modelled, provided that the spatial resolution of the 3D imaging technique covered the geometric scale of the mechanical responses of interest (deformation, cracking/microcracking, damage initiation/evolution, etc.) as well as that of the microstructural features.

The exhaustive quantification of microstructural features, such as size, shape, and spatial distribution, was realised by preparing a number of morphological parameters, which were used as design parameters in the microstructural optimisation framework (Step 3 in Fig. 1). Some objective functions were also defined so that the mechanical responses of interest were expressed as independent mathematical parameters (damage parameters, stress/strain, strength/elongation, crack length, lifetime, etc.). A combination of principal component analysis (PCA) and global sensitivity analysis (GSA) was then applied for the coarsening purpose to identify the set of final design parameters that would be effective for optimisation (Step 4 in Fig. 1).

The effectiveness of the proposed technique was validated and demonstrated for a wrought 2024 aluminium alloy in which irregularly shaped Al_2Cu particles coexisted with microscopic pores.

2.1. Design of numerical experiments

In standard surrogate modelling frameworks, how the experiments are designed is crucial. One of the most popular procedures for the design of experiments is Latin hypercube sampling [12]. In this method, the range for each design parameter is divided into a certain number of bins, and then data points are randomly allocated in the design space to statistically obtain a quasi-random sampling distribution. The main drawback of this for image-based numerical simulations is the difficulty of reconstructing realistic 3D microstructure models from a combination of all the design parameters. Therefore, in the sampling method adopted for this work, we randomly selected the regions of interest for the 3D image-based numerical simulations from the whole field of view in an experimentally obtained 3D image. The irregular and complex 3D microstructural features of a real-world practical material mean that a variety of microstructural features and patterns, in terms of species/phases, size, shape, and spatial distribution, are sampled in numerical models by random selection. The design parameters can reasonably cover a practically possible design space without the need for choosing an appropriate model size for the 3D image-based numerical simulation. This is because although design parameters should be spread apart as much as possible in order to capture the global trends of data dispersion in the design space, it is not necessary to allocate data points where they cannot physically exist in the materials (particles that are too small or too coarse, spatial distributions that are too uniform or too sparse, etc.).

Examples of the regions of interests used in the subsequent application are shown in Fig. 2. In this case, a unit box of 40 × 40 × 40 μm in size was extracted from a sufficiently wide field of view (approximately 600 × 600 × 1000 μm) of the high resolution synchrotron X-ray microtomography image. Five models were selected from 360,000 possible

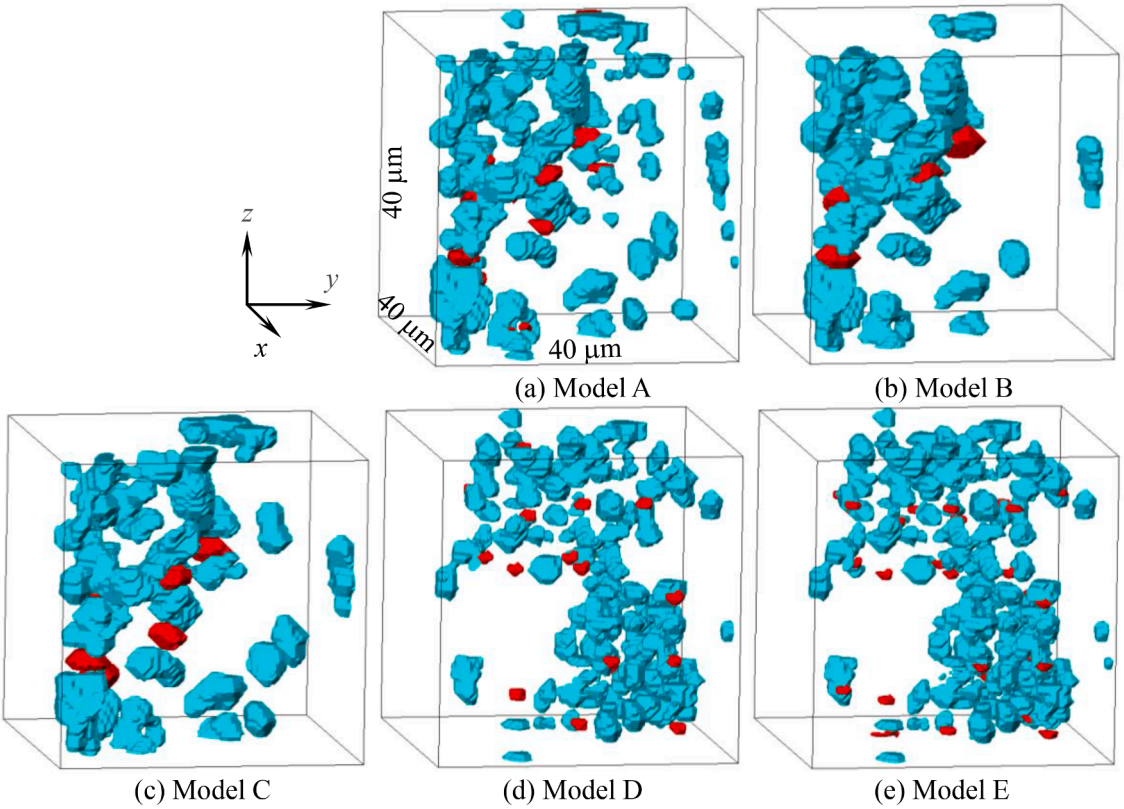

Fig. 2. 3D perspective views of the five 3D FEM models (Models A–E) used in the image-based numerical simulation. Only pores and particles are displayed, which are represented in red and light blue, respectively, and the underlying aluminium is not displayed.

microstructural patterns that were sampled by translating the unit box by 10 μm in the *x*, *y*, and *z* directions in the 3D image. Some microstructural features could be intentionally copied, eliminated, translated, or rotated, if necessary, in order to change the average size, morphology, orientation, volume fraction, spatial distribution pattern, etc. of the microstructures of interest for each model.

2.2. High-fidelity 3D imaging and image-based numerical simulations

It is assumed that a variety of discipline-specific simulations are assembled (fluid mechanics, heat transfer, solid mechanics, etc.) and either the continuum methods, such as the finite difference method, the boundary element method, the finite element method, etc. or the discontinuum methods, such as the discrete element method [13], are applied.

It is crucially important to generate high-fidelity 3D models of the irregular and complex microstructures so that the microstructural features and mechanical responses to be analysed are described with sufficient accuracy and fields of view. The realistic modelling of actual microstructural morphologies is made possible only when the spatial resolution and contrast resolution of the imaging system exceeds certain levels, taking into account the noise in 3D images. It should be noted that there is intrinsic trade-offs between spatial resolution and contrast, and spatial resolution and the field of view, and unnecessarily high spatial resolutions are often as bad as too low. It is, therefore, crucial when choosing the apparatus to take this into account.

2.3. High-fidelity quantification

The morphological parameters used for quantifying the size, shape, and spatial distribution of microstructural features in this study are summarized in Table S1. Since there are a variety of definitions for describing morphologically complex shapes, it would seem reasonable to prepare multiple parameters for expressing shapes in Table S1, such as orientation, aspect ratio, deviations from cubes or spheres, connectivity and surface complexity for particular features. Nine parameters were also prepared for expressing size (a large number that may even appear excessive). XCT often involves the visualization of internal structures that are relatively close to their effective spatial resolution due to limitations in the spatial resolution capacity of the devices used, whether from industrial-use scanners or synchrotron radiation XCT. For example, in the application in this study, an experimental set-up with a spatial resolution of 1 μm (the physical limit of the projection-type XCT) was employed to observe particles or pores of 1–10 μm in sphere-equivalent diameter. It should be noted that the volume or the sphere-equivalent diameter, which is directly calculated from the volume, enables accurate measurements when the spatial resolution level is much higher than the size of microstructural features of interest (e.g., 100 μm particles visualised by the 1 μm spatial resolution apparatus). When the thickness of flat particles is relatively close to the spatial resolution level of an imaging set-up, measuring particle size by the volume and sphere-equivalent diameter is susceptible to gross errors. On the other hand, drawing a bounding box, which is the smallest cuboid containing a particle, enables more accurate measuring of the height, width, and depth of particle sizes [1]. With this is mind, redundant parameters were prepared in morphological parameters that expressed the shape and the spatial distribution patterns, as shown in Table S1.

2.4. Coarsening design parameters

As noted in subsection 2.3, a large number of design parameters were used to express the morphological features of the microstructure in this study. Therefore, it was of crucial importance to screen out the design parameters with lower degrees of correlation. The coarsening process consisted of the following two steps: PCA for eliminating similarities in the set design parameters and GSA for selecting important design parameters that had a high degree of correlation with defined objective functions.

PCA is a popular linear dimensional reduction technique for data mining. PCA results can be represented with score and loading charts, where a score chart represents how the design parameters correspond to the variables of the principal component and a loading chart conveys how the design parameters contribute to the total variability of the first and second principal components [14]. Two or more design parameters that are close to each other form a small angle on a loading chart. The set of design parameters that is closer than a pre-determined threshold angle is eliminated leaving the design parameter with the longest distance from the origin having the strongest contribution.

GSA is a technique for apportioning the uncertainty in objective functions to the uncertainty in each design parameter [15]. The adjective "global" in GSA implies that all the design parameters are simultaneously variable, and the sensitivity is analysed over the entire range of interest for each design parameter. GSA is applied for selecting a limited number of design parameters with high Pearson correlation coefficients after the number of design parameters is reduced in the first step by applying PCA. The Pearson correlation coefficient, which is equivalent to the standardized regression coefficient in regression analysis, was used in this study. It quantifies the effect of the parameters on the model. In our case, $X = p_{\mathrm{i}}$ denoted the random variable for the i_{th} design parameter, and Y was the random variable representing the mechanical response (i.e. objective function). The partial correlation then quantified the degree of linear correlation between the parameter p_{i} and the mechanical response Y. The Pearson correlation was then given by

$$\rho_{p_i Y} = \frac{\sum_j \left((p_i)_j - \overline{p}_i\right)\left(Y_j - \overline{Y}\right)}{\sqrt{\sum_j \left((p_i)_j - \overline{p}_i\right)^2 \sum_k (Y_k - \overline{Y})^2}} \tag{1}$$

where $\overline{p}_i$ and $\overline{Y}_i$ are the means of p_{i} and Y, respectively. In this method, variables with large Pearson correlation values are considered more significant than those yielding small values. Values greater than 0.5 generally indicate significant correlations. However, parameters with Pearson correlation values less than 0.5 can be analysed for possible confounding factors.

2.5. Optimisation using a surrogate model

Surrogate models are built using data drawn from expensive models (image-based finite element simulations) that are able to predict the output at untried points in a design space. Amongst the several popular surrogate models available from past research, the support vector machine can effectively handle extremely high-dimensional data from a relatively small amount of sampling data [16]. The support vector machine outperformed compared with other optimisation methods (e.g., artificial neural networks), resulting in significant reductions in computational costs. The support vector machines were constructed using the libsvm-mat-3.25–1 Toolbox [17] and can be represented for input data ξ as

$$f(\xi) = \sum_{i=1}^{n} \alpha_i K(\xi, \xi_i) + b \tag{2}$$

where n is the number of data points, i indexes the samples, $K(\xi_i, \xi_j)$ is a kernel function for 2D data (ξ_i, ξ_j) that is based on Merer's theorem [18], and b is the offset of a hyperplane. In the proposed framework, the following two common kernels were applied:

$$\text{Polynomial}: \ K(\xi,\ \xi_i) = (\xi_i,\ \xi)^d \tag{3}$$

$$\text{Gaussian radial basis function}: \ K(\xi,\ \xi_i) = \exp\left(-\frac{\xi_i - \xi^2}{2\sigma^2}\right) \tag{4}$$

In this paper, the support vector machine was used with the infill sampling criterion shown in Fig. S1, which effectively alleviates computational burdens by further reducing the number of numerical trials needed to find the final solution. There are two criteria that were implemented to control the termination of the loop in Fig. S1. One is the criterion for convergence: The process is stopped when the change in the surrogate model (i.e. the accuracy of the model) falls below a specified threshold (i.e. 0.1 in this study). This implies that further sampling is unlikely to significantly improve results any more. The second criterion is the maximum number of iterations: The process is stopped after a fixed number of iterations (i.e. 5 in this study), the values of which can be set based on the computational budget.

2.6. General framework for model visualization and accuracy assessment

Since human brains are unable to efficiently grasp multi-dimensional output from surrogate models that are typically expected to be four or more dimensions (one objective function and more than three design parameters), we needed to exercise ingenuity for model visualization. In order to roughly evaluate the output from surrogate models, response surface methodology [19] was used to explore the relationship between an objective function and a couple of explanatory design parameters that were extracted from all the design parameters that survived the coarsening processes. The remaining design parameters that were not selected for drawing a response surface were kept constant at their average values. This approach is only an approximation, but such a model makes it easy to visualize the optimal and weakest microstructural features at a glance and determine how explanatory design parameters affect a response objective function of interest.

Although response surface methodology represents an efficient solution, it does not allow for direct interpretation of the positions of data points in space. Therefore, Radviz visualization [20], a more complicated non-linear visualization technique that displays multi-dimensional data with three or more parameters as a two dimensional projected graph, was used to provide a more accurate assessment of the surrogate model. With Radviz visualization, the design parameters to be visualized are presented as anchor points equally spaced along the perimeter of a unit circle. Data points are plotted inside the circle with their positions determined by equilibrium amongst imaginary springs that are linked to all the dimensional anchors. The stiffness of each spring is proportional to the value of the corresponding design parameter. Data points that are close to a specific anchor have higher values for the design parameters than for other data points. In such a way, the Radviz visualization method can project a n-dimensional data set into a 2D space, where the influence of each design parameter is interpreted as a balance amongst all the design parameters.

3. Application of the R4ME method to a practical purpose

3.1. Synchrotron microtomography image used for modelling

The effectiveness of the proposed technique was demonstrated with a wrought 2024 aluminium alloy for aerospace applications in which irregularly shaped coarse Al_2Cu particles coexisted with microscopic pores. A 3D tomographic image of microstructural features (particles and pores) was taken from past research (Material HH in reference [21]). A purchased wrought alloy was re-melted in ambient laboratory air. The alloy cast had a chemical composition of 4.447 Cu, 1.462 Mg, 0.452 Mn, 0.150 Zn, 0.170 Fe, 0.047 Si, 0.022 Ti, 0.012 Cr, 0.006 Zr, 0.003 Pb, 0.003 Ni, and balance Al in mass pct. The ingot was homogenized at 673 K for 28.8 ks, hot rolled at 673 K by 50 pct and cold rolled by 50 pct before applying a solution treatment at 768 K for 7.2 ks and an ageing treatment at 533 K for 86.4 ks. The total hydrogen content was measured by means of the vacuum fusion method, and was 0.72 cm^3 per 100 g of aluminium [21], which was expressed as the equivalent volume of hydrogen gas at 273 K and 1 atm. Some of the hydrogen had precipitated as spherical micro pores, as shown as red features in Fig. 2, with an average diameter of 2.8 μm, a number density of 163,700/mm^3, and a volume fraction of 0.27% [21]. Irregularly shaped Al_2Cu particles, comparable in size to the micro pores, were dispersed more densely than the micro pores as shown as blue features in Fig. 2, with an average diameter of 2.5 μm, a number density of 537,800/mm^3, and a volume fraction of 1.82% [21].

A high-resolution X-ray CT experiment was performed using the X-ray imaging beamline BL20XU of SPring-8 [21]. A sample rotation stage was positioned ~242 m from the X-ray source. A monochromatic X-ray beam with a photon energy of 20 keV generated by a liquid nitrogen-cooled Si (111) double crystal monochromator was used. An image detector consisted of a cooled 4000 (H) x 2624 (V) element CCD camera (effective pixel size of the camera: 5.9 μm), which was used in 2 x 2 binning mode, a single-crystal scintillator (Lu_2SiO_5: Ce), and a lens (20x). The image detector was positioned 55 mm behind the sample, thereby making the imaging system sensitive to phase modulation. In total, 1500 radiographs, scanning 180 deg, were obtained in 0.12 deg increments. Image slices were reconstructed from a series of projections based on the conventional filtered backprojection algorithm. The in-situ observation of a tensile test was performed, and damage and fracture behaviour is displayed in ref. [21]. An isotropic voxel with a 0.5-μm edge and a substantial spatial resolution of 1.0 μm was achieved in the reconstructed 3D image, which was calibrated such that the linear absorption coefficients of micro pores, aluminium, and particles fell within an 8-bit grey scale range.

3.2. Image-based finite element simulations

In addition to the model preparation already described in the latter half of Section 2.1, STL meshes of particles and micro pore surfaces were obtained with volume rendering software together with an outer cubic geometry of 40 μm in size that were loaded on PATRAN, a pre-processor for finite element simulations. Surface triangular meshes with an aspect ratio higher than five were eliminated, and the particle and aluminium regions in models were divided using tetrahedral elements. In this way, 3D FE models that consist of the matrix, particles and pores can be successfully created. For example, the numbers of tetrahedral elements and nodes in Model A in Fig. 2(a) are 78,756 and 116,919, respectively, and those for the other models ranged within ± 5% of these values. The particles and the matrix aluminium were assumed to be elastic and elasto-plastic, respectively. Young's moduli and Poisson ratios of the matrix and the particles and were set to be 69 GPa/0.33 and 105 GPa/0.34, respectively [22]. A true stress-true strain curve for the 2024 aluminium matrix was taken from the reference [23], which was fitted by the Ramberg-Osgood equation. Note that the simulation was fully implicit, and neither fracture criterion nor damage model was utilised.

The finite element simulations of tensile tests were performed using the commercial finite element simulation software Marc/Mentat. All the nodes on the edge ($z = 0$) are fixed along z-direction, while tensile displacement of 2 μm (i.e. a uni-axial tensile strain of 5%) is applied for the nodes on the other side ($z = 40$ μm). Since it is not realistic because the effects of particle/pore agglomeration can be amplified, no periodic boundary condition is applied. The other three nodes at the corners except for the origin ($y = 0$) were also fixed along y-direction to prohibit rigid rotational motion of the model. The Typical examples of the computation results are shown in Fig. 3 as the distributions of normal stress, equivalent plastic strain, and stress triaxiality on a specific cross-section in Model A, which were used as the three objective functions in Section 3.3. Significant local variations in the three mechanical quantities were observed in the computation results, as shown in Fig. S2, which demonstrates the elevation of particle stress where coarse particles were irregularly shaped.

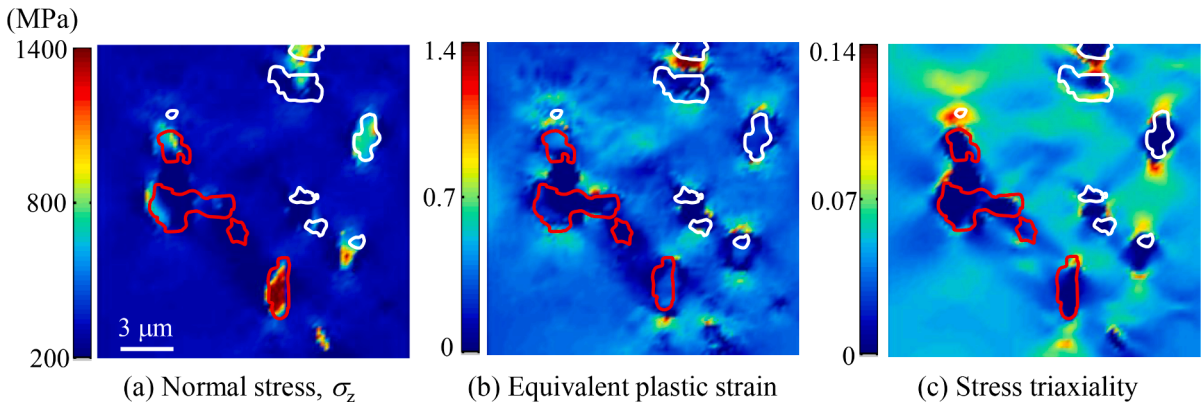

Fig. 3. Magnified views of the output of finite element analysis on virtual cross-sections. Equivalent plastic strain, stress triaxiality, and normal stress σ_z, are shown, which correspond to the objective functions, I_1, I_2, and I_3, respectively, in the final optimization. Red and white lines denote pores and particles, respectively.

3.3. *Objective functions and design parameters*

All the design parameters are explained in Section 2.3 along with a comprehensive list in Table S1. There were wide variations in size, shape, and spatial distributions of particles, as shown in Fig. 4, in which extreme examples of particle size and shape were quantified with the design parameters O and f_4. The left and right particles in Fig. 4(a) and (b) have design parameter values close to 0 and 1, respectively, after normalization, while the upper middle and lower middle particles have design parameter values close to their averages.

Three objective functions, I_1, I_2, and I_3, were defined in order to evaluate the damage evolution from particles from various viewpoints (i.e. damage initiation and growth, particle and matrix, stress and strain, etc.). It has been reported that particle damage directly contributed to the ductile fracture behaviour of the material [21]. I_1 and I_2 expressed the mechanical conditions for micro void formation initiated from the fracture of particles, whereas I_3 was associated with micro void growth. I_1 was the maximum value of the maximum principal stress in particles. It was assumed to be directly associated with the criterion for particle fracture. I_2 was the maximum value of the equivalent plastic strain of the

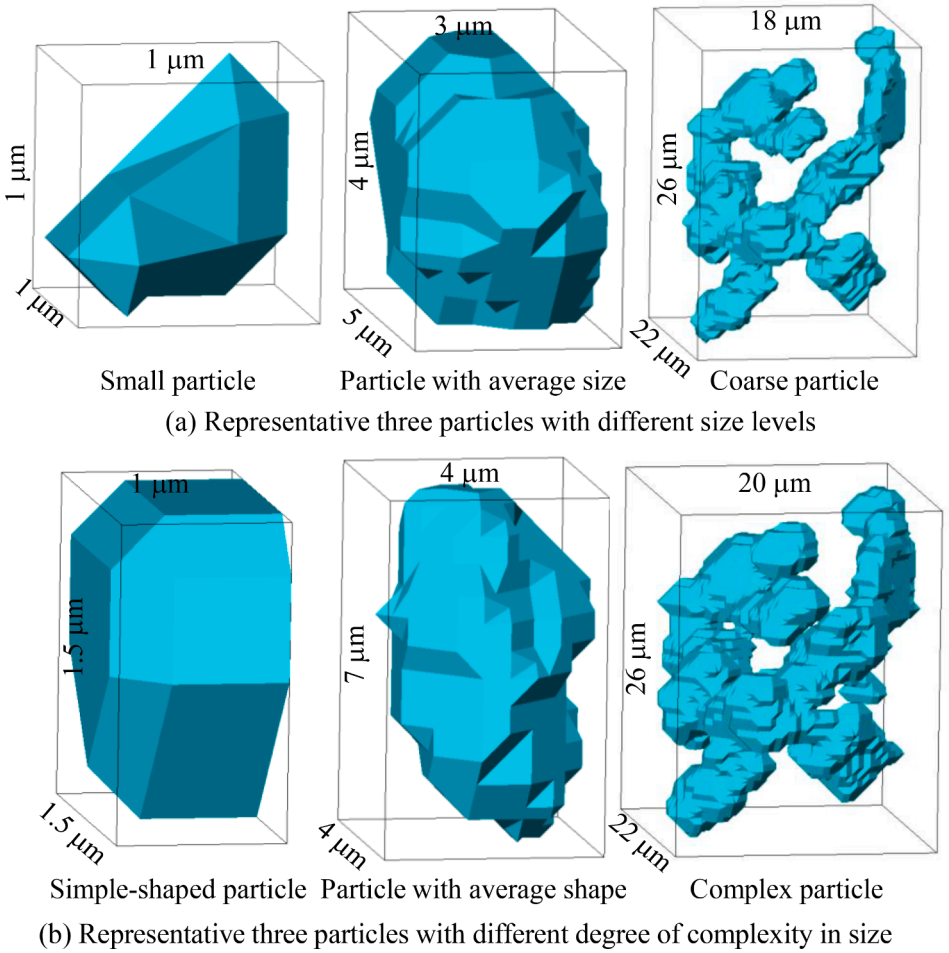

Fig. 4. Examples of representative particles by (a) size and (b) shape, which have been selected from the original 3D image according to the morphological quantification results. Small, medium, and coarse particles in (a) are referred as particles A, B, and C in Fig. S3.

matrix aluminium in the vicinity of a particle. Significant elevation of internal stress was expected inside particles where plastic strain was localized in the underlying matrix. I_3 was defined as the maximum value of stress triaxiality of the matrix in the vicinity of a particle. According to the Rice and Tracy model, high stress triaxiality corresponds to the lateral expansion of voids during fracture [24].

Prior to the coarsening processes, all of the objective functions and design parameters were normalized to be between 0 and 1. This was done so that a 99% confidence interval was the upper limit of the normalized range (i.e., unity) in each figure, as shown in Fig. S3. The locations of the three particles displayed in Fig. 4(a) are shown as particles A, B, and C in Fig. S3 for reference.

3.4. Coarsening results

The threshold angle value in the PCA process was set to be 5°. Two or more design parameters that were close to each other within this angle are listed in Table S2, and at least one of the design parameters was eliminated in each couple of parameters. As a result, the number of design parameters was reduced from 41 to 14, and the loading chart was plotted again using the remaining 14 design parameters, as shown in Fig. 5. The majority (about 57%) of the remaining design parameters (p_6, p_8, θ, E, f_3, f_4, O_4, f_{10}) denoted particle shape, followed by design parameters on particle size (about 36%: L, O, T, D, G). Only one design parameter that described the spatial distribution of particles, d_m, survived. The design parameters f_3, f_4, O_4, and f_{10} expressed the magnitude of elongated shapes in some forms. The third moment invariant, p_8, could be used to show how complex and less ellipsoidal-like particles with the same aspect ratio were [25]. The design parameters p_6, θ, and E were associated with irregularities, orientation of the first principal axis, and connectivity of particles, respectively. The design parameters L/T and O enabled size measurements based on the bounding box and three principal axes, respectively, which could be assumed as approximate evaluations, whereas D fully utilized the high spatial resolution of the X-ray CT image through volume measurements. Geodesic distance, G, expressed a morphometric feature that reflected both the size and shape complexity of particles.

Further coarsening was performed by applying the GSA process, and

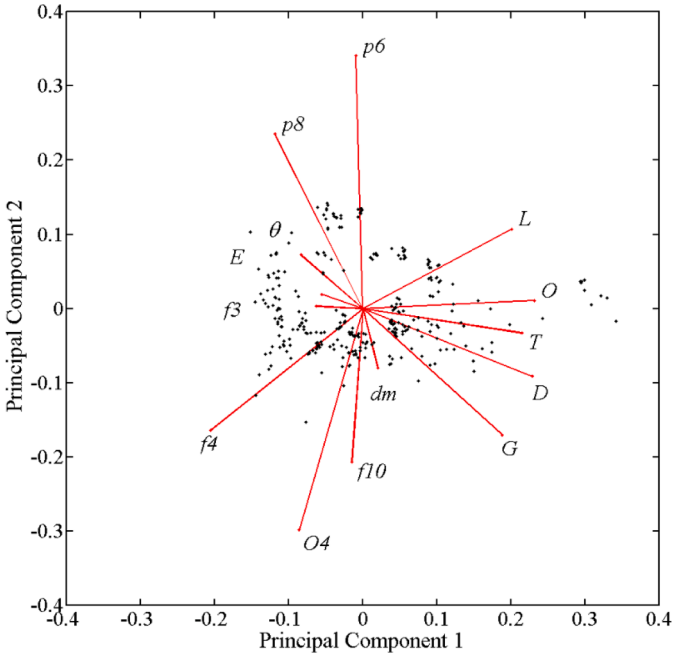

Fig. 5. Principal component score distribution for the remaining 14 design parameters after applying the PCA process.

the results are shown in Fig. 6. Four design parameters were selected for each objective function, leaving at least one parameter from each category (i.e., size, shape, and spatial distribution). The largest design parameter in remaining design parameters was selected as the fourth parameter for each objective function to reflect the importance of category with a higher Pearson correlation coefficient level. For I_1, I_2, and I_3, (O, f_4, T, d_m), (p_3, p_7, G, d_m), (l_2, d_m, p_2, O) were selected, respectively, as the sets of input design parameters for the surrogate models, where O, T and G are fundamentally associated with size, d_m and l_2 express spatial distribution and the other four parameters quantify shape. In general, the value of the Pearson correlation coefficient r was between −1 and +1, with positive values indicating positive relationships and vice versa. According to Evans, the strength of correlation is moderate, weak, and very weak for r with values of 0.40–0.59, 0.20–0.39, and 0–0.19, respectively [26]. Therefore, it can be concluded that a relatively reasonable correlation was identified for I_1, while only a weak correlation was obtained for I_3. This is probably because I_1 expressed the direct criterion for micro void formation (the maximum principal stress in particles), whereas I_3 was the rather indirect criterion for void growth (the stress triaxiality of the matrix). I_2 was intermediate in the level of relevancy, resulting in an intermediate level of correlation between the objective function and the selected design parameters. It can be inferred for I_1 that D and L, which have moderate correlation levels, may be adopted as the fifth and sixth design parameters. The physical meanings of D and L are however rather close to that of already adopted T. It can therefore be assumed that such modification would not be so influential on optimisation results. Due to space limitations, the results for I_1 are shown hereafter in this study.

Fig. 7 shows the distributions of the four design parameters selected for I_1 between the respective normalized ranges (0–1) together with the distributions of the data points in the design space expressed in 2D for all possible combinations. The former and the latter are expressed as bar graphs and x-y plots, respectively. The design parameters reasonably cover almost the entire design spaces for d_m-O, f_4, and T (d_m: average distance within each cluster based on the K means method, O: average length of three principal axes, f_4: deviations from spherical shape, and T: thickness of minimum volume bounding box). For the other three combinations a remarkable agglomeration of rather narrow stripes is seen. This is partly because there was an inherent tendency in the 2D design spaces for f_4-T and f_4-O that coarse particles exhibited more irregular and complex shapes, whereas fine particles were rather spherical. In addition, O and T were rather close by definition (i.e. size), which is also confirmed by the experimental data shown in Fig. 5. Therefore, it can be inferred that coverage of the design space of the four design parameters was sufficient to perform a realistic statistical analysis based on the global trends of actual data dispersion in the design space.

3.5. Optimisation results

Of all the 300 particles, 238 particles were used as training data for generating a surrogate model, and 62 particles were used as test data. Fig. 8 shows the comparison between the surrogate model generated for I_1 and the results of the finite element simulation for the tested 62 particles. It can be seen from Fig. 8 that the surrogate model can provide highly accurate predictions. Average percentage error is about 0.20, and 66% of the output data points showed percentage error values less than 0.2 (50% showed less than 0.1). It can be considered as rather small relative error for this very complex issue. It can therefore be concluded that the surrogate model can provide reasonably accurate predictions much more cheaply than evaluating the true function by repeating the very expensive and laborious image-based numerical simulation almost unceasingly. On the other hand, 4.8% and 1.6% of the output data points showed considerable underestimation and overestimation with percentage error values greater than 0.3, respectively. Of course, the number of particles can be increased by preparing additional simulation

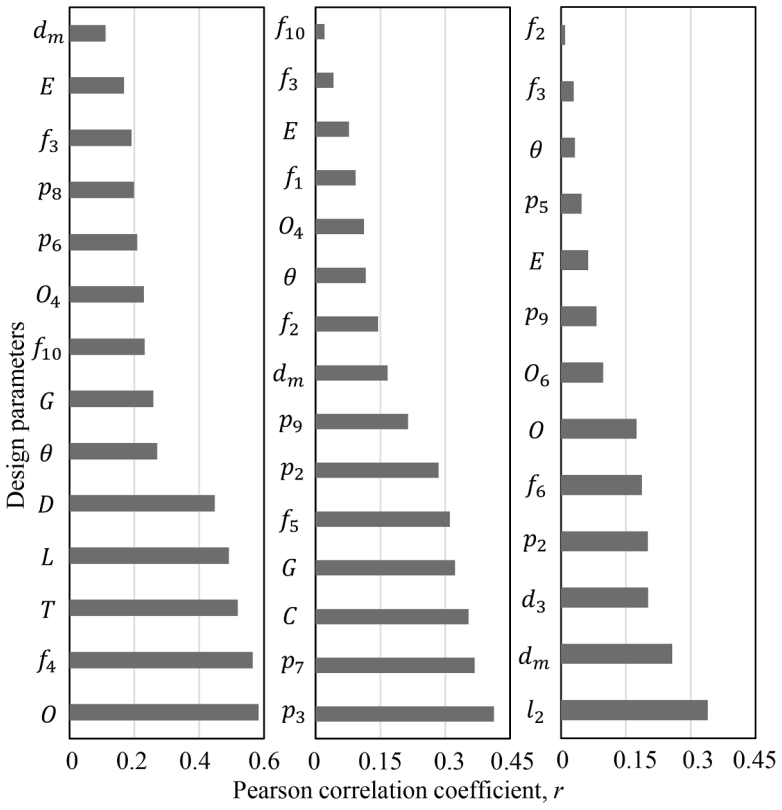

Fig. 6. Results of the global sensitivity analysis, which represent the Pearson correlation coefficients for objective functions I_1, I_2, and I_3 .

models to improve this. The goal of surrogate modelling would not however be to perfectly reproduce the true function, but rather to provide good-enough approximation for limited input data. Therefore, measures to improve accuracy, such as optimising the ratio between the number of teacher data and that of test data, and increasing the number of particles per model to the extent that there are no substantial interference effects amongst particles, are also likely to be necessary.

3D contour maps of the objective function I_1 were predicted by the surrogate model. Two sets of the three design parameters were selected to show 3D design spaces, and the remaining parameter was fixed at the average values in Fig. 9(a) and (b) (d_m= 0.231 and T = 0.447 for (a) and (b), respectively). The optimal and weakest particles for particle damage are expressed in blue and red in Fig. 9, respectively. Actual size, shape, and spatial distribution values of the predicted optimal particle are shown in Table 1 for reference. Manufacturers can control the mechanical properties of the 2024 aluminium alloy so that there are as many particles as possible that have four design parameter values that are close to these values. It can be surmised from Fig. 9 that the optimal particle with the highest resistance against damage is rather small (O) and spherical (f_4) and relatively sparsely dispersed (d_m), and its longitudinal axis is perpendicular to the loading direction (T). It is interesting to note that according to the results of the analysis, the smallest and most independent (the one does not belong to a cluster) particle with a spherical shape was not necessarily strong. This means all the four selected parameters had mutual dependency and could not vary by fixing the other parameters to be constant. For example, clustered particles are sometimes small and rather spherical, whereas sparsely dispersed particles are sometimes coarse and irregularly shaped. It can be also seen in Fig. 9 that the blue region spreads widely in terms of d_m. This is simply because of its low Pearson correlation coefficient.

The Radviz chart in Fig. 10 is more informative and shows some of the underlying structure of the dataset. Fig. 10 shows how that when the surrogate model was used to estimate particle stress (strong particles lower than 1743 MPa, intermediate particles between 1743 and 2937 MPa, and weak particles higher than 2937 MPa), the three classes are almost separated. The data points predicted with the surrogate model coincided well with the computation results of the finite element simulation except for a limited number of data points that were closer to d_m (i.e. the design parameter for spatial distribution) for the strong and intermediate particles. This is attributable to the relatively low Pearson correlation coefficient of d_m shown in Fig. 6(a).

From the position of the data points in Fig. 6(a), we were able to make some conclusions about the values of the shown attributes. For example, the weak particles were close to the centre position of all the four attributes, which means that all four design parameters were important for damage initiation. Compared to the stronger particles in Fig. 10(a) and (b), the weak particles in Fig. 10(c) are closer to the design parameters associated with particle size. This implies that the dependency of in-situ particle strength on its size (T and O) is of crucial importance to understand the degradation of particle strength. On the other hand, the data points were more agglomerated in the vicinity of f_4 (shape parameter) and d_m (spatial distribution parameter) as the strength of particles increased. This implies that particle shape and spatial distribution are more crucial for suppressing the elevation of internal stress inside particles than particle size.

4. Insights inspired from the present application

The conventional approach in materials science and engineering attempts to improve the properties of materials by employing a limited amount of testing combined with microstructural and fracture surface analyses. However, it sometimes yields room for interpretation by engineers and researchers because of gaps in existing information, and numerical simulations and modelling complement experimental data by

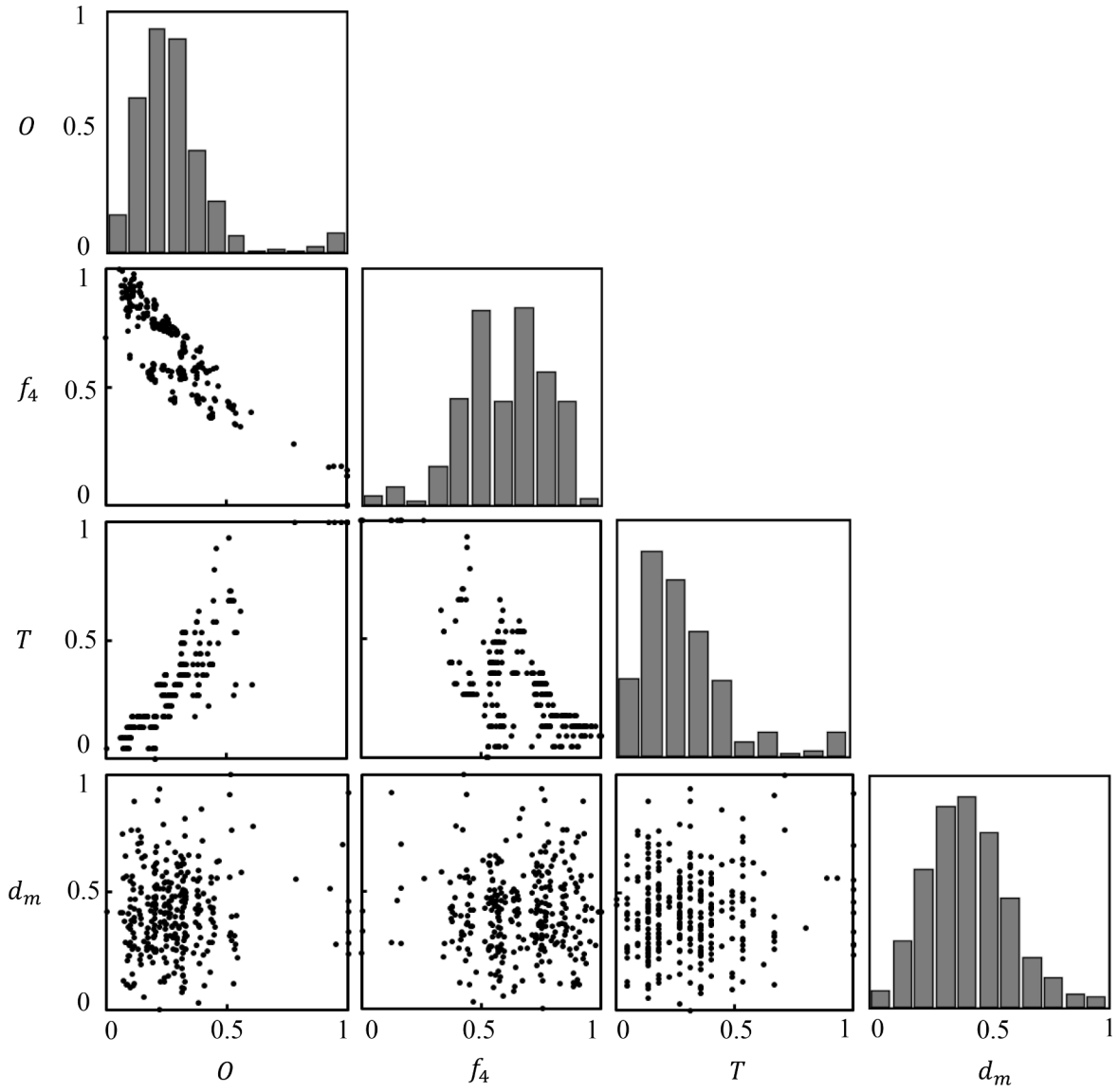

Fig. 7. Distributions of the selected four design parameters for all the 300 particles analysed. Distribution of the data is shown in 2D design space between each pair of the four parameters.

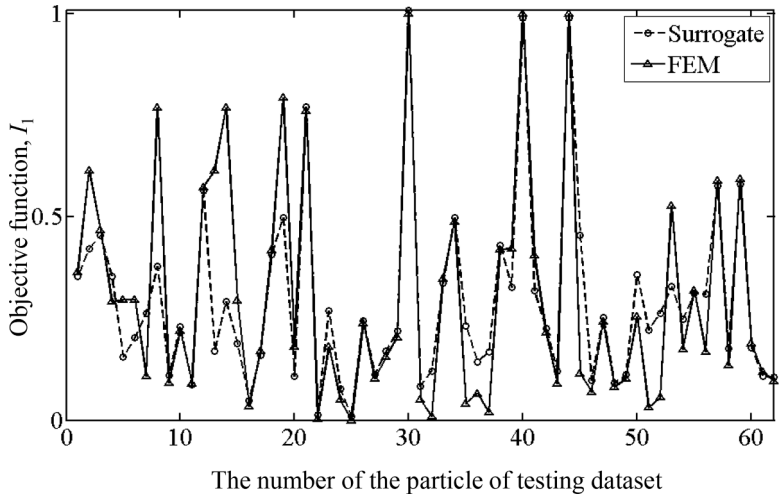

Fig. 8. Comparison between the input (the computation results of a finite element simulation) and the created surrogate model. The result for the objective function I_1 is shown. .

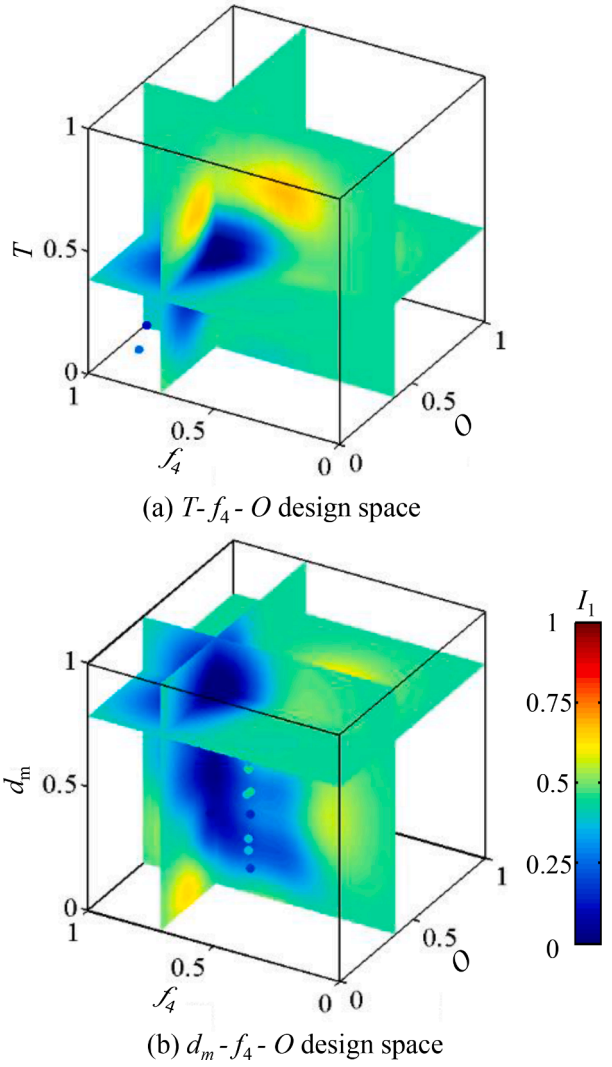

Fig. 9. 3D contour maps of the objective function I_1 predicted by the surrogate model. Three design parameters were selected to show a 3D design space with the remaining parameter fixed at average values in (a) and (b) (d_m= 0.231 and T = 0.447 for (a) and (b), respectively). The computation results of the finite element simulation are also shown as dots.

Table 1
Predicted optimum values for the four selected design parameters for the objective function I_1.

Design parameter	O	f_4	T	d_m
Category	Size	Shape	Size	Distribution
Optimum value	2.89 mm	0.65	5.53 mm	5.27 mm

providing information that is not produced with experimental approaches. For example, the 3D image-based numerical simulations in this study provided equivalent plastic strain, stress triaxiality, and normal stress values. The latter two were not obtained from the XCT experiments. Equivalent plastic strain was obtained by analysing the XCT data. In this case, the maximum value for the equivalent plastic strain in the vicinity of a particle was computed, and the detailed distribution was not obtainable experimentally.

It should be noted that the quantity of tomographic data was prodigious. The number of microscopic and nanoscopic features embedded in a single 3D image sometimes amounts to tens or hundreds of thousands. It is evident that averaging and standardization, which are often taken in the conventional approaches, would considerably diminish the importance of such high-fidelity 3D images even without taking a look at such examples shown in Fig. 3. The same is true with high computational cost image-based numerical simulations in which a huge number of complex microstructural features are captured and reflected in models. By employing 3D image-based numerical simulations, it is possible to fill in design space gaps that are not covered by presently available material microstructures by artificial modification of the material microstructures. For example, the combination of the four finally selected design parameters appears to locate in the vicinity of the outer edge of the actual microstructure in the design space of Fig. 7. The behaviour of such geometrically rare particles can be easily overlooked in the conventional experiments. Numerical simulations and modelling approaches complement experimental data by providing information that is not produced with experimental approaches. High-resolution 3D imaging of microstructures and the morphologies of cracks or damage enables the creation of 3D image-based numerical models that faithfully reproduce the actual behaviour of local materials. The variety of behaviour of such a huge number of complex microstructural features is infinite. Therefore, it is hard to grasp this by simply viewing experimental data or simulation results. Experimental and numerical data often include the five V's (volume, variety, velocity, veracity, and value). In this regard, it can be assumed to be big data.

The methodology proposed in this paper enables presenting the weakest microstructural feature and extracting the dominant factors from such massive amounts of data. And it provides new findings, insights, and reasonable interpretations of complex phenomena, leading to improvements in the characteristics of materials through microstructural optimization. It is possible to move away from a conventional intuitive understanding of phenomena to a logical interpretation corroborated by the huge amount of data. If we would like to reach findings similar to Table 1 and Figs. 9 and 10 even if qualitatively by employing the conventional approach, a thorough parametric analysis is needed by repeating image-based numerical simulations many times. Considering that it took roughly half a year for the preparation and computation of the five models shown in Fig. 2, the time necessary for such analysis would be astronomical.

We have seen such examples in Fig. 9 and 10 for practical aluminium alloys. For example, most of the design parameters associated with particle spatial distribution did not survive, and the solely surviving d_m exhibited a low correlation coefficient, contrary to the expectation that particle clustering is detrimental [27]. It can be inferred that weak particles were identified to be coarse and probably did not cluster due to the size range of clustered particles and the relatively low internal stress in clustered particles because of the effects of interaction. In addition, the contribution of the four selected design parameters (d_m, O, f_4 and T) varied in Fig. 10 depending on the level of particle strength. For example, the damage initiation of weak particles was correlated more strongly with the two design parameters associated with particle size than the other two parameters, whereas particle shape and spatial distribution became more important with the increase in particle strength. It implies that in order to eliminate the weakest points in a material with moderate strength, particle size should be mainly controlled. But when strength/ductility is enhanced to the maximum extent possible for the material with a higher strength level, particle shape and spatial distribution should be considered. It would be impossible to obtain such findings if the damage initiation behaviour of a huge number of particles with complex microstructural feature is experimentally observed.

The data from recent experiments using XCT of in-situ observations of materials under external disturbance have been getting even richer. And because of the progress in advanced analytical and measurement technologies, we have performed more multi-modal analyses, such as polycrystalline visualization for crystallographic orientation measurements and grain boundary visualizations [1,4,6] and small angle X-ray scattering for nanoscopic microstructure evaluations [28]. First, the importance of such leading-edge analysis technologies can be assessed

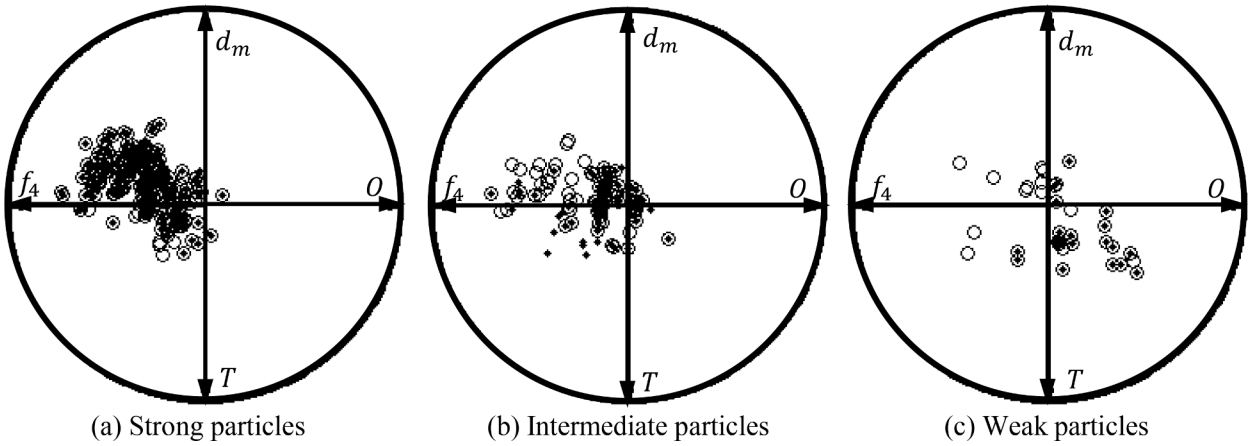

Fig. 10. Radial visualization for the assessment of the accuracy of the surrogate model (black dots), which is compared with the computation results of the finite element simulation. The result for the objective function I_1 is shown. (a) Strong particles with maximum normal stress in the z direction lower than 1743 MPa, (b) particles with intermediate strength of between 1743 and 2937 MPa, and (c) weak particles higher than 2937 MPa.

by applying these techniques. A wide variety of highly correlated data is then selected to analyse in a number of ways, which leads to the correct understanding of phenomena. When information about objective functions is experimentally determinable, this methodology can be applied to various issues without requiring numerical simulations.

A 3D image-based numerical simulation utilises the particular microstructural features embedded in a single specimen, and, in principle, it only leads to universal understanding after multiple repetitions. This is equivalent to testing a material multiple times. However, this is rarely done due to the high computational costs. The methodology proposed in this paper compensates for such shortcomings and delivers the full potential of 3D image-based numerical simulations. In general, in order to utilize 3D or 4D images and the 3D image-based numerical simulations based on them, we need experienced personnel that can understand, interpret, and utilize the data. Deep insights into materials science and profound academic knowledge are indispensable. There are insufficient numbers of trained personnel who can combine high levels of materials science knowledge with data processing abilities. The methodology proposed in this paper enables researchers and engineers to reach identical conclusions without data cleansing when an appropriate goal for data utilization is set and a sufficient number of design parameters are prepared. It is well known that data quality must meet the following five requirements: completeness, uniqueness, validity, accuracy, and consistency. It is also well understood that defects, duplications, inconsistencies, and failures in data lead to erroneous conclusions. Therefore, to enhance data quality, data bugs must be fixed through data cleansing. The methodology proposed in this paper inherently does this through design parameter coarsening. The strength of correlation analysis after GSA and radial visualization assessment of the surrogate model also provide features to validate the feasibility and effectiveness of the present surrogate-based optimization method.

5. Conclusion

The methodology introduced in this study required high-fidelity 3D imaging and 3D image-based numerical simulations based on high-fidelity 3D images. Some objective functions were first defined so that the mechanical responses of interest were expressed as independent mathematical parameters that were visible or measureable in experiments and were computable in 3D image-based numerical simulations. High-fidelity quantification of microstructural features of interest, which were as a matter of course correlated with the prepared objective functions, was then performed after preparing a number of design parameters that expressed morphological and crystallographic features, etc. A very large number of design parameters were used at this stage. Therefore, it was of crucial importance to screen out the design parameters with lower degrees of correlation in the subsequent coarsening processes. Surrogate-based microstructural optimization was then executed with the support vector machine algorithm and the infill sampling criterion, with which we could quantitatively identify the optimal and weakest microstructural features together and understand the multi-dimensional response of objective functions over wide ranges of selected design parameters.

The effectiveness of the proposed methodology for the practical 2024 aluminium alloy with irregularly shaped particles has been shown. The three objective functions, which were correlated with particle damage, were defined so that the strength and ductility that originated from ductile fractures were optimized. Although the number of design parameters, which quantitatively express the size, shape, and spatial distribution of Al_2Cu particles, was initially 41, it was finally reduced to four during the two-step coarsening process in which similarities in the set of design parameters and the degree of correlation with defined objective functions were considered. The surrogate model provided highly accurate predictions, and the size, shape, and spatial distribution values of the optimal and weakest particles were successfully identified. It was demonstrated that the optimal particle was small, spherical, and sparsely dispersed, and its longitudinal axis was perpendicular to the loading direction. However, it was also established that the smallest and most independent particle with a spherical shape was not necessarily strong, with implications about the nature of particle clustering (relatively small and spherical particles were clustered and vice versa). It was also concluded that the dependency of in-situ particle strength on size was of crucial importance for weaker particles. However, particle shape and spatial distribution were more crucial for stronger particles for suppressing particle internal stress than particle size.

This shows that the proposed methodology offered a cost-efficient solution for microstructural designs involving 3D high-fidelity simulations, which was not achieved with existing approaches for developing materials. In addition, when the number of microscopic and nanoscopic features associated with the phenomenon of interest were sufficiently shown in 3D images (e.g., the condition for design parameters) and the information about objective functions was experimentally determinable (e.g., the condition for objective functions), then the methodology in this study could be applied to various issues without requiring numerical simulations.

Declaration of Competing Interest

The authors declare that they have no known competing financial interests or personal relationships that could have appeared to influence

the work reported in this paper.

Acknowledgements

The synchrotron experiments were performed with the approval of JASRI through the proposal numbers 2013B1027, 2020A1796, and 2020A1084. This work was supported by JSPS KAKENHI Grant Numbers JP17H01328 and JP21H04624, the Japan Science and Technology Agency (JST) through the project Core Research for Evolutional Science and Technology (CREST) (Grant number JPMJCR1995), and the Light Metal Educational Foundation.

Supplementary materials

Supplementary material associated with this article can be found, in the online version, at doi:10.1016/j.actamat.2023.119188.

References

[1] H. Toda, X-Ray CT, Hardware and Software Techniques, Springer Nature Singapore, Singapore, 2021.
[2] S. Carmignato, W. Dewulf, R. Leach, Industrial X-Ray Computed Tomography, Springer, Berlin, 2017.
[3] P.J. Withers, X-ray nanotomography, Mater. Today 10 (2007) 26–34.
[4] H.F. Poulsen, Three-dimensional X-ray Diffraction microscopy, Mapping Polycrystals and Their Dynamics (Springer Tracts in Modern Physics), Springer, Berlin, 2004.
[5] W. Ludwig, E.M. Lauridsen, S. Schmidt, H.F. Poulsen, J. Baruchel, J. Appl. Crystallogr. 40 (2007) 905–911.
[6] H. Toda, T. Kamiko, Y. Tanabe, M. Kobayashi, D.J. Leclere, K. Uesugi, A. Takeuchi, K. Hirayama, Diffraction-amalgamated grain boundary tracking for mapping 3D crystallographic orientation and strain fields during plastic deformation, Acta Mater. 107 (2016) 310–324.
[7] C.J. Kamp, S. Zhang, S. Bagi, V. Wong, G. Monahan, A. Sappok, Y. Wang, Ash permeability determination in the diesel particulate filter from ultra-high resolution 3D X-ray imaging and image-based direct numerical simulations, SAE Int. J. Fuels Lubr. 10 (2017) 608–618.
[8] M.J. Baker, P.G. Young, G.R. Tabor, Image based meshing of packed beds of cylinders at low aspect ratios using 3d MRI coupled with computational fluid dynamics, Comp. Chem. Engng. 35 (2011) 1969–1977.
[9] L. Qian, H. Toda, K. Uesugi, M. Kobayashi, T. Kobayashi, Direct observation and image-based simulation of three-dimensional tortuous crack evolution inside opaque materials, Phys. Rev. Lett. 100 (2008), 115505.
[10] M. Saadatfar, M. Mukherjee, M. Madadi, G.E. Schröder-Turk, F. Garcia-Moreno, F. M. Schaller, S. Hutzler, A.P. Sheppard, J. Banhart U. Ramamurty, Structure and deformation correlation of closed-cell aluminium foam subject to uniaxial compression, Acta Mater. 60 (2012) 3604–3615.
[11] M.A.S. Qidwai, A.C. Lewis, A.B. Geltmacher, Using image-based computational modeling to study microstructure–yield correlations in metals, Acta Mater 57 (2009) 4233–4247.
[12] S. Motavalli, Review of reverse engineering approaches, Comp. Ind. Engng. 35 (1998) 25–28.
[13] A. Manouchehrian, M.F. Marji, M. Mohebbi, Comparison of indirect boundary element and finite element methods, Front. Struct, Civ. Eng. 6 (2012) 385–392.
[14] I.T. Jolliffe, Principal Component Analysis (Springer Series in Statistics), Springer Nature, 2002.
[15] A. Saltelli, M. Ratto, T. Andres, F. Campolongo, J. Cariboni, D. Gatelli, M. Saisana, S. Tarantola, Global Sensitivity Analysis. The Primer, John Wiley & Sons, 2007.
[16] J. Shawe-Taylor, S. Sun, A review of optimization methodologies in support vector machines, Neurocomputing 74 (2011) 3609–3618.
[17] C.C. Chang, C.J. Lin, LIBSVM, A library for support vector machines, ACM Trans. Intell. Syst. Technol. 2 (2011) 1–27, 2727.
[18] B. Scholkof, A.J. Smola, Learning with Kernels, MIT Press, Cambridge, MA, 2002.
[19] G.E.P. Box, K.B. Wilson, On the experimental attainment of optimum conditions, J. R. Stat. Soc., Ser. B 13 (1951) 1–45.
[20] P. Hoffman, G. Grinstein, K. Marx, I. Grosse, E. Stanley, DNA visual and analytic data mining, in: The Proceeding of the IEEE Visualization, 1997, pp. 437–441. Phoenix, AZ.
[21] H. Toda, H. Oogo, K. Horikawa, K. Uesugi, A. Takeuchi, Y. Suzuki, M. Nakazawa, Y. Aoki, M. Kobayashi, The true origin of ductile fracture in aluminum alloys, Metall. Mater. Trans. A: Phys. Metall. Mater. Sci. 45 (2014) 765–776.
[22] N.M. El Chazly, M.M. Farag, Inhomogeneity of plastic deformation and fracture modes in two-phase alloys, Mater. Sci. Eng. 55 (1982) 29–38.
[23] A. Hosokawa, H. Toda, R. Batres, H. Li, O. Kuwazuru, M. Kobayashi, H. Yakita, Ductile fracture via hydrogen pore mechanism in an aluminum alloy; quantitative microstructural analysis and image-based finite element analysis, Mater. Sci. Eng., A 671 (2016) 96–106.
[24] J.R. Rice, D.M. Tracey, On the ductile enlargement of voids in triaxial stress fields, J. Mech. Phys. Solids 17 (1969) 201–217.
[25] J.P. Mac Sleyne, J.P. Simmons, M. De Graef, On the use of moment invariants for the automated analysis of 3D particle shapes, Modelling and Simul, Mater. Sci. and Eng. 16 (2008), 045008.
[26] J. Evans, Straightforward Statistics for the Behavioral Sciences, Brooks/Cole Publishing, Pacific Grove, CA, 1996.
[27] J. Segurado, C. Gonza´lez, J. LLorca, A numerical investigation of the effect of particle clustering on the mechanical properties of composites, Acta Mater. 51 (2003) 2355–2369.
[28] S. Lin, H. Okuda, Y. Nishikawa, S. Sakurai, T. Kabe, H. Masunaga, Nondestructive nanostructure analysis of Al/Al–Zn interdiffusion layer by quantitative SAXS tomography, Mater. Trans. 62 (2021) 1673–1676.